Journal of Constructional Steel Research 144 (2018) 106–118

Contents lists available at ScienceDirect

Journal of Constructional Steel Research

Local-flexural interactive buckling of standard and optimised cold-formed steel columns

Jun Ye [a,b,*], Seyed Mohammad Mojtabaei [a], Iman Hajirasouliha [a]

[a] Department of Civil Engineering and Structural Engineering, The University of Sheffield, Sheffield, UK
[b] Department of Architectural and Civil Engineering, University of Bath, Bath, UK

ARTICLE INFO

Article history:
Received 25 August 2017
Received in revised form 8 January 2018
Accepted 9 January 2018
Available online 2 February 2018

Keywords:
Columns
Finite element
Interaction buckling
Local buckling
Optimisation

ABSTRACT

This paper aims to study the interaction of local and overall flexural buckling in cold-formed steel (CFS) channels under axial compression. Detailed nonlinear FE models were developed and validated against a total of 36 axial compression tests on CFS plain and lipped channel columns with pin-ended boundary conditions. The numerical models incorporated the non-linear stress-strain behaviour of CFS material and enhanced properties of cold-worked corner regions obtained from coupon tests. The effects of initial geometric imperfections of the specimens measured by a specially designed set-up with laser displacement transducers were also taken into account. The developed FE models produced excellent predictions of the ultimate strength of the specimens obtained from experimental tests. The validated FE models and experimental results were then used to assess the adequacy of the effective width method in Eurocode 3 (EC3) and Direct Strength Method (DSM) in estimating the design capacity of a wide range of conventional and optimised design CFS channel column sections. The results indicate that Eurocode 3 provides conservative predictions (on average 21% deviation) for the compressive capacity of plain and lipped channel sections, while in general DSM predictions are more accurate for lipped channels. A comparison between FE predictions and tested results show that geometric imperfections can change the FE predictions by up to 20% and 40%, respectively, for lipped and plain channel columns, while the strain hardening effect at the rounded corner regions of the cross-sections is negligible. The results also confirmed that the proposed numerical model is able to provide a consistent and reliable prediction on the efficiency of a previously proposed optimisation methodology.

Notation

b, b_e Gross and effective width of the plate
c Lip width
h Web height
t_{eff} Effective thickness
L_e Length of the column
I Coil width of the steel sheet
A_s Area of the edge stiffener
I_s Effective second moment of area of the stiffener
f_y Material yield stress
E Young's modulus
ψ Stress ratio
ρ Reduction factor on the plate width
σ_{cr} Elastic local buckling stress
$\sigma_{cr,\,s}$ Elastic critical buckling stress for an edge stiffener
K Spring stiffness per unit length
χ_d Reduction factor for flexural buckling of the stiffener
λ_p, λ_d, λ Local, distortional and global buckling slenderness ratio in effective width method
$\lambda_{p,\,red}$ Updated λ_p in each iteration
λ_l, λ_{dl}, λ_c Non-dimensional local, distortional and global buckling slenderness in the DSM
N_{Ed} Design value of the compression load
$N_{b,\,Rd}$ Design buckling resistance of a compression member
$M_{b,\,Rd}$ Design pure bending moment resistance around weak axis
e_N Shift of centroid
ΔM_{Ed} Additional bending moment due to shift of centroid
P_y Compressive yield load
P_{crl}, P_{crd}, P_{cre} Elastic critical force for local, distortional and global buckling modes
P_{nl}, P_{nd}, P_{ne} Axial strength for local, distortional and global buckling modes, respectively
P_n Ultimate axial strength of the column
P_{u1}, P_{u2}, P_{u3} Predicted axial strengths considering the effects of strain hardening of the material in the corner regions, measured geometric imperfections, and both.

* Corresponding author at: Department of Civil Engineering and Structural Engineering, The University of Sheffield, Sheffield, UK.
E-mail addresses: j.ye@bath.ac.uk, zjuyejun@gmail.com (J. Ye).

https://doi.org/10.1016/j.jcsr.2018.01.012

1. Introduction

In common practice, cold-formed steel (CFS) structural elements have traditionally been employed as secondary load-carrying members such as stud walls, roof purlins, wall girts and cladding. However, in a more recent trend, CFS members are also increasingly being employed as primary structural elements in low- to mid-rise multi-storey buildings [1] and CFS portal frames with short to intermediate spans [2,3]. Compared to hot-rolled members, CFS thin-walled members offer several advantages, such as a high strength for a lightweight, a relatively straightforward manufacturing process, a high flexibility in obtaining various cross-sectional shapes, and an ease of transportation and faster construction. However, as a result of the limitations of the manufacturing process, CFS components usually have <6–8 mm thickness, which makes them susceptible to local, distortional and global buckling, as well as their interactions. The typical buckling modes of a lipped channel are illustrated in Fig. 1.

The theoretical aspects of local-flexural interactive buckling were first established by Van der Neut [4] on the basis of an elastic idealized column with two flanges supported along both longitudinal edges by infinitely thin webs. This early work, in combination with Van der Neut's later paper [5], demonstrated that the capacity of CFS columns is sensitive to both local and global imperfections, especially when the critical stresses of both buckling modes are of the same level. However, due to the inherent weaknesses of thin-walled cross-sections and their complex buckling modes, the accurate prediction of the buckling and post-buckling behaviour of CFS elements is relatively challenging. Finite Element Analysis (FEA) has been widely used in the past to predict the non-linear behaviour of CFS elements. Compared with physical experiments, FEA is relatively inexpensive and time efficient, especially when a parametric study of cross-section geometry is involved. In addition, FEA is more suitable and convenient for studies involving geometric imperfections and material nonlinearity of structural members, which could be difficult to investigate through physical tests.

In one of the early attempts, Young and Yan [6] developed a nonlinear FE model to investigate the compressive strength of fixed ended CFS columns, using four node shell elements with five degrees of freedom per node. Reduced integration was used (SR4) in combination with linear perturbation analysis 'BUCKLE' to incorporate imperfection effects. Based on experimental results on CFS fixed-ended lipped channel columns, Young [7] used a nonlinear inelastic FE model to investigate the effect of inclined edge stiffeners on ultimate axial capacity. Similarly, Yan and Young [8,9] experimentally and numerically studied the ultimate capacity of fixed-ended CFS channel columns with complex stiffeners. SR4 element type in ABAQUS [10] was used by taking into account initial geometric imperfections and material non-linearity. In another study, Zhang et al. [11] conducted an experimental test program on pin-ended CFS columns with perpendicular and inclined edge stiffeners and developed FE models using four-node shell element type with six degrees of freedom at each node in ANSYS [12]. The rigid region at each end of the column elements was modelled with a reference point, where rotations around both strong and weak axis of the end sections were allowed. Wang et al. [13] conducted a series of experimental tests on pin-ended columns with complex cross-sectional edge and intermediate stiffeners and the results were compared with the FE models similar to one proposed by Zhang et al. [11]. In a recent study, Ayhan and Schafer [14] used an experimentally verified numerical model in ABAQUS [10] to obtain moment-rotation curves and characterize the backbone response curve of CFS members in monotonic bending. Based on both experimental and numerical results, a series of new local/distortional slenderness based design equations were proposed to provide a rapid estimation of the buckling and post-buckling behaviour of CFS members.

To obtain more efficient design solutions, Ma et al. [15] and Ye et al. [16] developed a practical optimisation framework for CFS channel cross-sections in compression or bending based on the effective width method adopted in Eurocode 3 [17–19]. In their framework, the plate slenderness limits and the limits on the relative dimensions of the cross-sectional components set by the Eurocode as well as a number of construction and manufacturing constraints were taken into account. The results showed that, in general, optimised CFS sections possess relatively higher axial and flexural strength compared to other standard prototypes. However, even though available design equations developed in Eurocode 3 are well accepted for the calculation of strength of CFS members, their ability to estimate the increasing/decreasing trend in optimisation process is still questionable. On the other hand, the adequacy and reliability of the optimisation method adopted by Ma et al. [15] and Ye et al. [16] should be validated by experimental results or accurate numerical models before they can be widely used in practice.

This paper aims to investigate the local-flexural interactive buckling behavior and ultimate capacity of CFS standard and optimised plain and lipped channel columns by developing detailed FE models in ABAQUS [10]. The results of a companion experimental investigation including 36 tests on CFS channel columns [20,21], which were all failed by the interaction of local instability and flexural buckling about the minor axis, are used to validate the FE models. Compared to previous studies, the main advantage of the developed models is to incorporate the non-linear stress-strain behaviour of CFS material and enhanced properties of cold-worked corner regions (based on coupon tests) as well as the measured initial geometric imperfections. The validated models are then used to assess the adequacy of Eurocode 3 design guidelines [17–19] and Direct Strength Method (DSM) for the design and optimisation of CFS columns considering local/distortional and global buckling modes.

2. Eurocode 3 design procedure

Prior to the description of the numerical study, a brief induction is presented here to explain the EC3 design guidelines to consider local, distortional and global buckling, their interaction and inelastic reserve around minor axis in the compressive strength of CFS members.

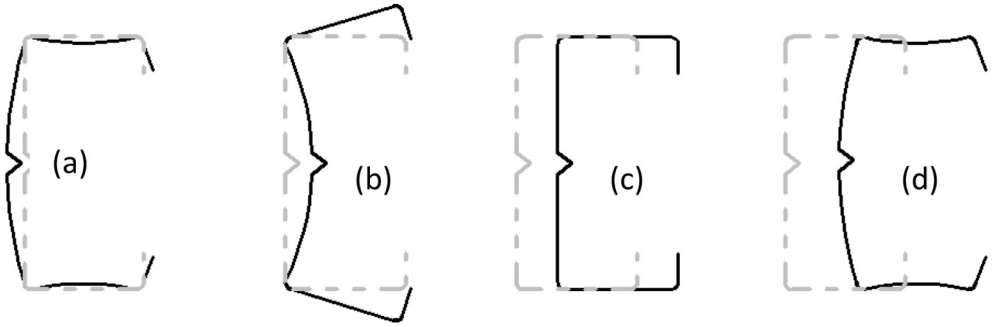

Fig. 1. Buckling modes of a lipped channel: (a) local, (b) distortional, (c) global and (d) local-global interactive modes.

2.1. Local buckling

The phenomenon of local buckling is characterized by the flexural deformation of a plate without movement of the intersection lines between adjacent plates, as shown in Fig. 1 (a). The EN1993-1–5 [17] uses an effective width concept (see Fig. 2(a)) to design thin-walled CFS cross sections for local buckling. According to EN1993-1–5 [17], the effective widths of internal and outstand compression elements are given by:

$$\rho = \frac{b_e}{b} = \begin{cases} \frac{1}{\lambda_p}\left(1-\frac{0.055(3+\psi)}{\lambda_p}\right) & \text{for internal compression element} \\ \frac{1}{\lambda_p}\left(1-\frac{0.188}{\lambda_p}\right) & \text{for outstand compression element} \end{cases} \quad (1)$$

with

$$\lambda_p = \sqrt{\frac{f_y}{\sigma_{cr}}} \quad (2)$$

In Eq. (1) ρ is the reduction factor on the plate width, while b and b_e are the total and the effective width of the plate, respectively. The slenderness ratio λ_p relates the material yield stress f_y to the elastic local buckling stress of the plate σ_{cr} and ψ is the stress ratio of an individual plate.

As illustrated in Fig. 2(b), the effective width of outstand compression elements can be calculated by Eq. (2). An improved approach is also included in Annex D of EC3 [18] to calculate the effective width as well as the effective thickness of the flange element of a plain channel. If the maximum compression happens at the free longitudinal edge (see Fig. 2(c)), the effective width (b_e) and effective thickness (t_{eff}) are calculated as follows [18]:

$$b_e = 0.42b \quad (3)$$

$$t_{eff} = (1.75\rho - 0.75)t \quad (4)$$

2.2. Distortional buckling

Distortional buckling of CFS members is related to a distortion of the shape of the cross-section, without including the deformations related to the local buckling (see Fig. 1(b)). As a result, distortional buckling is always associated with the displacement of one or more of the intersection lines or the ends of the section out of their original positions. Distortional buckling can also be interpreted as global (flexural or flexural-torsional) buckling of an effective stiffener. According to the latter point, the design for distortional buckling in EC3 [18] is based on the assumption that the effective parts of an edge stiffener(Fig.3 (a)) behave as a strut element continuously supported by elastic springs of stiffness K along its centroid axis. Fig. 3 (b) shows the adopted model for a continuously supported strut under compression. The buckling behavior of the section can then be studied by considering an equivalent strut on an elastic foundation with critical buckling stress calculated from Eq.(5):

$$\sigma_{cr,s} = \frac{2\sqrt{KEI_s}}{A_s} \quad (5)$$

where K is the spring stiffness per unit length, A_s and I_s are the area and effective second moment of area of the stiffener. The flexural buckling resistance of the stiffener is then obtained by multiplying a reduction factor χ_d, which is defined in Fig. 3(c).

It is worth noting that EC3 considers the interaction of the local and distortional buckling modes by reducing the thickness of the effective parts of the flange stiffener. Also, the local buckling plate slenderness ratio λ_p of the flange and lip is updated considering the distortional buckling mode using the following equation:

$$\lambda_{p,red} = \lambda_p\sqrt{\chi_d} \quad (6)$$

For each step, the effective width of the plate will be refined until convergence. While this iteration is optional in EC3 [18], previous studies showed that in some cases it can considerably affect the actuary of the results [20,21].

2.3. Global buckling

Global buckling is characterized by the rigid body movements of the whole CFS, where the cross section rotates and translates without any distortion in shape (see Fig. 1(c)). For members in compression, the global buckling resistance is determined based on a non-dimensional slenderness ratio:

$$\lambda = \sqrt{\frac{A_{eff}\cdot f_y}{P_{cre}}} \quad (7)$$

where P_{cre} is the elastic critical force for global buckling mode based on the gross cross-sectional properties and A_{eff} is the effective area of the cross-section calculated from Sections 2.1 and 2.2.

2.4. Beam-column design

The local buckling of pinned-end channel columns can shift the centroid of the effective area relative to the center of gravity of the gross cross section [22]. The shift of effective centroid (e_N) can induce an additional bending moment ($\Delta M_{Ed} = N_{Ed}\cdot e_N$), which should be considered in the design process. The Clause 6.2.5 of EN1993-1–3 [18] recommends an interaction formula to consider the interaction between axial force and bending moment in beam-column elements:

$$\left(\frac{N_{Ed}}{N_{b,Rd}}\right)^{0.8} + \left(\frac{N_{Ed}\cdot e_N}{M_{b,Rd}}\right)^{0.8} \le 1 \quad (8)$$

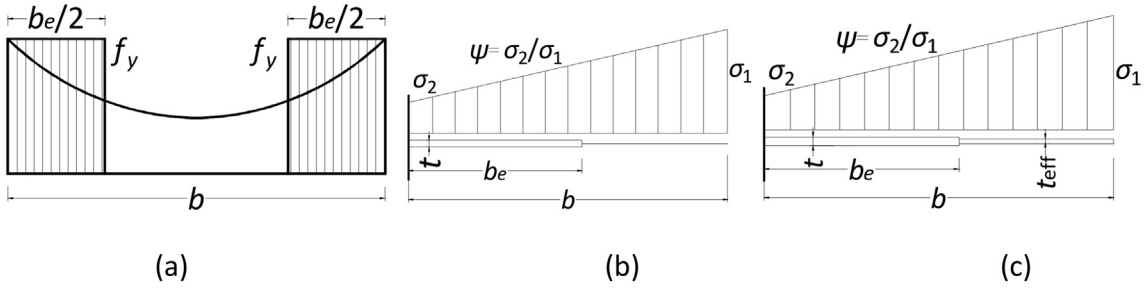

Fig. 2. Local buckling with (a) effective width concept (b) effective width of outstand compression element according to EC3 Part 1–5 [17] and (c) effective width/effective thickness of outstand compression element according to Annex D of EC3 Part 1–3 [18].

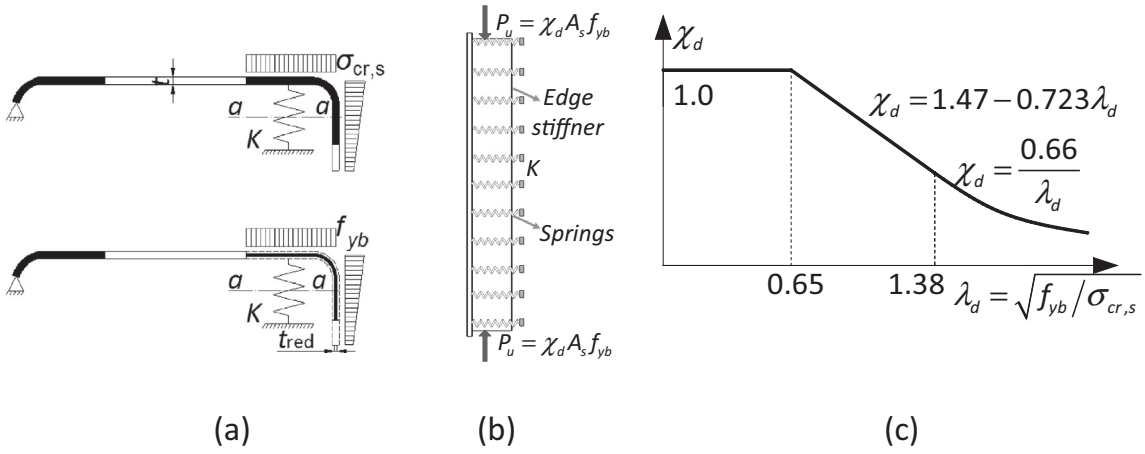

Fig. 3. Distortional buckling model: a. flange with edge stiffener; b. flexural buckling of edge stiffener as a strut on elastic foundation; and c. flexural buckling curve for edge stiffener.

where $N_{b,\,Rd}$ is the design buckling resistance of a compression member and $M_{b,\,Rd}$ is the design bending moment resistance around the weak axis of the cross-section.

It should be noted that to design CFS channel columns, the Annex E of EN1993-1–5 [17] can be also used, which calculates the effective area of the section based on the actual compressive stress level σ_{com} caused by the combination of compression and bending on the effective area of the cross-section (Clause 4.4(4) of EN1993-1–5 [17]). This calculation requires an iterative procedure in which the stress is determined at each step from the stresses calculated on the effective cross-section defined at the end of the previous step until full convergence is attained. In this study, both of the above-mentioned methods are used to estimate the axial strength of conventional and optimised CFS channel columns and the accuracy of the results are assessed based on experimental results.

2.5. Inelastic reserve capacity

In case of bending moment is applied about the weak axis in a CFS channel section, the neutral axis is quite often located eccentrically. For a CFS column, the additional bending moment due to the shift of effective centroid (e_N) can induce compression in the web of a lipped channel section, as shown in Fig. 4. The initial yielding therefore takes place in the tension part of the flange, and subsequently spreads into the web, resulting in an inelastic reserve strength in the cross-section. Based on EC3 [18], part of this inelastic reserve strength can be utilised by using the effective partially plastic section modulus $W_{pp,\,eff}$. Using a bilinear stress distribution, the effective widths of a web b_{e1} and b_{e2} in Fig. 4 (a) are obtained based on a total plate width of $2y_c$ and a stress ratio $\psi = -1$, where y_c is the distance between the neutral axis and the top flange as shown in Fig. 4(b).

The location of neutral axis from the top flange can be found by using the equilibrium of the forces derived from bilinear stress distribution shown in Fig. 4 (c):

$$y_c = \frac{1}{2}(b_p - c_e - h_e) \tag{9}$$

where h_e, b_p and c_e are the web effective width, flange length and lip length, respectively. Then the ultimate moment of the section can be calculated based on the stress resultants in Fig. 4(c) as:

$$\begin{aligned} M_u = 2f_y t\Big\{ & h_e y_c + \frac{2}{3}y_c^2 - \frac{b_{e2}}{2y_c}(y_c - b_{e1} - b_{e2}) \\ & \times \left[\frac{1}{3}(y_c - b_{e1}) + \frac{2b_{e2}}{3}\right] - \frac{y_c - b_{e1}}{2y_c}(y_c - b_{e1} - b_{e2}) \\ & \times \left[\frac{2}{3}(y_c - b_{e1}) + \frac{1}{3}b_{e2}\right] + y_p\left(y_c + 0.5y_p\right) + c_e\left(y_c + y_p\right)\Big\} \end{aligned} \tag{10}$$

where y_p is the length of the web that exhibits full yield stress, as shown in Fig. 4(b). It is worth to note that Eq. (10) is also applicable to plain channels when the effective length of the lip c_e is set to be zero.

3. Direct Strength Method (DSM)

The Direct Strength Method (DSM) proposed in AISI [23] is an alternative to the traditional effective width method to predict the load carrying capacity of CFS members. This method integrates a computational stability analysis into the design process. In a first step, the elastic local (P_{crl}), distortional (P_{crd}) and global (P_{cre}) buckling loads are determined by using finite strip method. Using these elastic buckling loads and the load at first yield, the strength is then directly predicted based on a

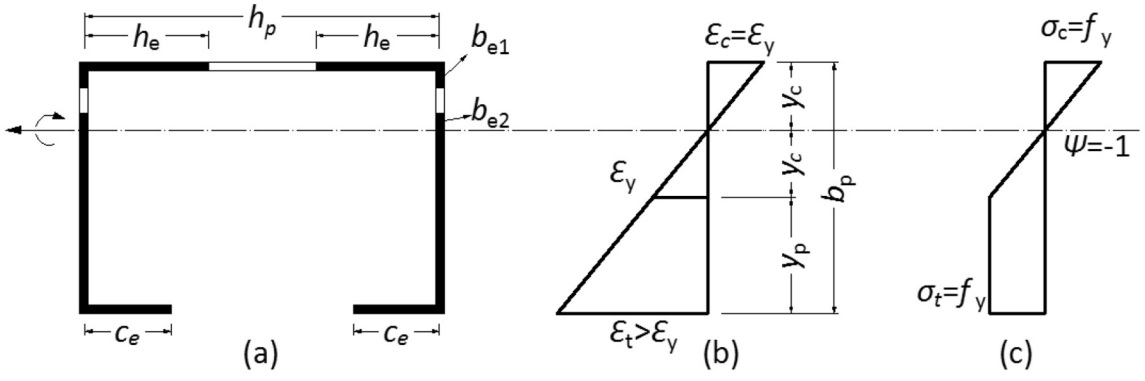

Fig. 4. Strain and stress distribution of a lipped channel bending around weak axis and with initial yielding at tension edge.

series of simple empirical equations. While calculation of the effective properties can be tedious for complex CFS cross-sections, only gross section properties are needed in the DSM. The elastic buckling loads of CFS members can be calculated using software such as CUFSM [24]. More detailed information on modal decomposition based on the Finite Strip Method is provided by Ádány and Schafer [25,26].

The equations for calculating the axial strength for global buckling in AISI [23] are presented in terms of the compressive yield load $P_y = A_g \cdot f_y$ and the non-dimensional slenderness ratio $\lambda_c = \sqrt{P_y/P_{cre}}$, where:

$$\begin{cases} P_{ne} = \left(0.658^{\lambda_c^2}\right) P_y & for\ \lambda_c \le 1.5 \\ P_{ne} = \left(\dfrac{0.877}{\lambda_c^2}\right) P_y & for\ \lambda_c > 1.5 \end{cases} \tag{11}$$

The nominal axial strength for local buckling can be determined by considering local–global interaction and its related local–global slenderness non-dimensional ratio $\lambda_l = \sqrt{P_{ne}/P_{crl}}$, where:

$$\begin{cases} P_{nl} = P_{ne} & for\ \lambda_l \le 0.776 \\ P_{nl} = \left[1 - 0.15\left(\dfrac{P_{crl}}{P_{ne}}\right)^{0.4}\right]\left(\dfrac{P_{crl}}{P_{ne}}\right)^{0.4} P_{ne} & for\ \lambda_l > 0.776 \end{cases} \tag{12}$$

Finally, the nominal axial strength corresponding to the distortional buckling is calculated as a function of the distortional buckling slenderness ratio $\lambda_{dl} = \sqrt{P_y/P_{crd}}$, using the following equations:

$$\begin{cases} P_{nd} = P_y & for\ \lambda_{dl} \le 0.561 \\ P_{nd} = \left[1 - 0.25\left(\dfrac{P_{crd}}{P_y}\right)^{0.6}\right]\left(\dfrac{P_{crd}}{P_y}\right)^{0.6} P_y & for\ \lambda_{dl} > 0.561 \end{cases} \tag{13}$$

The ultimate axial strength of the column P_n is then determined by calculating the minimum value of the axial strength values obtained from Eqs (11) to (13) as follows:

$$P_n = min\{P_{ne}, P_{nl}, P_{nd}\} \tag{14}$$

4. Optimisation of CFS beam-columns

The optimum cross-sections used in this paper, are designed based on an optimisation framework which was previously developed the authors [27] for the purpose of generating more efficient yet practically useful CFS elements. The proposed optimisation framework takes the ultimate strength of CFS elements as objective function. In this study, the cross-sections were designed according to EC3 [18] while the dimensions complied with the Eurocode geometrical requirements as well as a number of manufacturing and practical constraints. A Particle Swarm Optimisation (PSO) algorithm was used to solve the nonlinear optimisation problem. The total developed length (coil width) and the thickness of the cross-section (and consequently the total amount of material) were kept constant during the optimisation process. In order to apply the optimisation framework to pin-ended CFS columns, the following objective function (derived from Eq.(8) in Section 2.4) needed to be maximized:

$$N_{Ed} = \left(\frac{1}{\left(1/N_{b,Rd}\right)^{0.8} + \left(e_N/M_{b,Rd}\right)^{0.8}}\right)^{1.25} \tag{15}$$

In the above equation, $N_{b,Rd}$ and $M_{b,Rd}$ denote the member resistances in pure compression and pure bending about the minor axis, respectively, while e_N is the shift of the effective centroid caused by local/distortional buckling. The column capacity N_{Ed} thus accounts for the additional bending caused by the shift of the effective centroid, as described in Section 2.4. It should be noted that in the calculation of the cross-sectional pure compression capacity $N_{b,Rd}$ and pure bending capacity $M_{b,Rd}$ about the minor axis, the local/distortional buckling interaction (in Section 2.2) and inelastic reserve capacity (in Section 2.5) were taken into consideration and iterations were carried out to convergence.

The following design constraints were also considered in the optimisation process:

$$b/t \le 60, c/t \le 50, h/t \le 500 \tag{16}$$

$$0.2 \le c/b \le 0.6 \tag{17}$$

$$c \le 25 \tag{18}$$

Eq. (16) denotes the limits on the width-to-thickness ratios set by EC3 [18], while Eq. (17) is set according to Clause 5.2.2 of the Eurocode. Eq. (18) is a practical manufacturing constraint, which was determined in consultation with the industrial partner of the project, who had limited flexibility in adapting the existing cold-rolling line to product new cross-sectional shapes. While these constraints might prevent a global optimum solution being reached, they illustrate very well the capabilities of the previously proposed optimisation framework to incorporate various practical limitations.

In this study, the above optimisation algorithm was conducted for pin-ended columns with a length $L_e = 1.5$ m. This was deemed to be practical as it represents the effective length of typical studs with a storey height of 3 m and one row of intermediate rods at mid-height. Additional optimisations were also conducted for columns with $L_e = 1.0$ m and $L_e = 2.0$ m and the results showed that the optimum cross-sectional dimensions did not vary significantly within these three different lengths.

The nominal dimensions of the cross-sections for the numerical study in this paper are presented in Fig.5. All the dimensions in this figure are defined by the outer to outer surface. The four types of cross-sections were labelled A–D, followed by the nominal length of the column in *mm* and 'a', 'b' or 'c' to indicate repeated testing. The cross-section A is a standard commercially available cross-section, which provided a basis for comparison. Section B is the optimum solution with the highest axial load capacity, subject to the design constraints presented in Eqs. (16) to (18). Section C is a standard plain channel, while section D is a lipped channel section with an intermediate depth between sections A and B and with randomly chosen dimensions. As it was mentioned before, all cross-sections have the same nominal thickness ($t = 1.5$mm) and coil width ($l = 337$mm), and therefore use the same amount of material.

5. Reference experimental tests

The results of an experimental programme conducted by the authors were used as a reference to validate the numerical models developed in this study. A total of 36 axial compression tests on CFS channels with three different lengths (1 m, 1.5 m and 2 m) and four different cross-sections as shown in Fig. 5 were conducted under a concentrically applied load and pin-ended boundary conditions [20,28]. The initial geometric imperfections of the specimens were measured using a specially designed set-up with laser displacement transducers. Material tests were also carried out to determine the tensile properties of the flat parts of the cross-sections, as well as the cold-worked corner regions. For each cross-section, one coupon was taken along the centre line of the web and another one along the centre line of the flange. Corner coupons were also cut from the rounded corner zones. These corner coupons were tested in pairs to avoid eccentric loading. The tests were conducted in accordance with the specifications of the relevant European standard ISO 6892-1 (CEN 2009) [29]. These coupon test data are used in this study to investigate the effect of cold-working

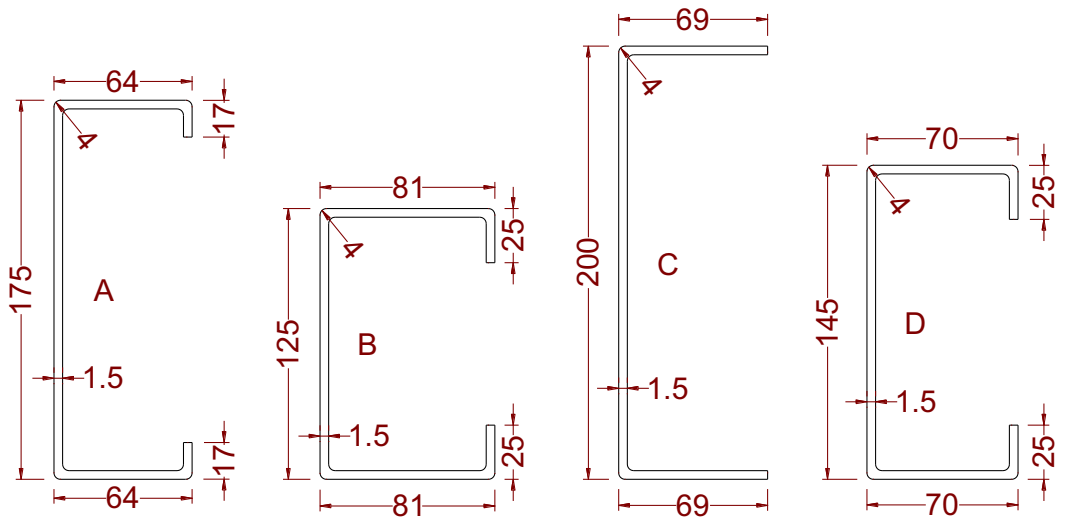

Fig. 5. Nominal cross-sectional dimensions.

process on the structural performance of CFS columns. The details of the reference experimental tests are provided in references [20,21].

6. Numerical modeling

6.1. Material model

The inelastic properties of CFS material were found to have significant effects on the ultimate capacity and post-buckling behavior of CFS elements [30]. Table 1 lists the values of the Young's modulus (E), the 0.2% proof stress ($\sigma_{0.2\%}$) and the tensile strength (σ_u) obtained from the coupon tests (see Section 5) for each tested specimen.

For example, Fig. 6 compares the engineering and the true stress-strain curves of a flat (A01F) and a pair of corner coupons (A03C and A04C). The results indicate that the 0.2% proof stress of the corner coupon is around 24% higher than the flat coupon in the same section. It should be noted that previous studies by Huang and Young [31] on dynamic and static stress–strain curves of coupon specimens showed that the stress is reduced by around 5–8% at both yield and ultimate strengths during the static drop, which is also called "stress relaxation". Therefore, in this study the static stress–strain curves are calculated from the dynamic stress–strain curves by removing the dynamic effects of the tensile test machine [20,31]. The results for both flat and corner zones of the members were then incorporated into ABAQUS [10] using the true stress vs true strain curve calculated from the following equations:

$$\sigma_{true} = \sigma(1+\varepsilon) \tag{19}$$

$$\varepsilon_{true} = \ln(1+\varepsilon) \tag{20}$$

where σ and ε are the measured engineering stress and strain based on the original cross-sectional area of the coupon specimens. It is worth noting that the plastic components of the true stress-strain curves shown in Fig. 6 were employed as input for the material model ABAQUS [10].

Table 1
Tensile properties of flat segments and corner regions.

Sections	Coupon	Type	E(MPa)	$\sigma_{0.2\%}$(MPa)	σ_u(MPa)
A1500-a	A01F	Flat	196,057	447.0	599.6
	A02F	Flat	195,355	448.5	599.1
	A03C	Corner	221,076	525.8	614.2
	A04C				
B1500-a	B01F	Flat	196,194	440.3	606.9
	B02F	Flat	203,486	441.2	594.9
	B03C	Corner	211,164	529.6	613.3
	B04C				
C1500-b	C01F	Flat	208,443	453.1	609.6
	C02F	Flat	205,302	459.0	621.5
	C03C	Corner	218,921	530.7	592.4
	C04C				
D1500-a	D01F	Flat	200,226	453.9	611.8
	D02F	Flat	193,743	448.5	603.2
	D03C	Corner	205,742	525.6	600.0
	D04C				

6.2. Boundary conditions

Four types of cross-sectional shapes were considered including a commercially available standard lipped channel; two optimised lipped and plain channel sections and a complementary lipped channel as introduced in Section 4 (see Fig. 5). In a companion study, a total of 36 axial compression tests were conducted using all these cross sections with three different lengths (1 m, 1.5 m and 2 m) and pin-ended boundary conditions about the minor axis. Fig. 7 (a) shows the experimental test set up used for the axial compression tests. The distance between the horizontal axis of the hinge and the top surface of the plate was measured to be 44 mm. More information about the experimental tests can be found in reference [20,21].

In the FE models, the hinge assemblies were modelled as 38 mm deep solid blocks with an arc-shaped groove with 6 mm in depth, which was allowed to rotate about the longitudinal axis of the roller. The radius of the cylinder roller was designed to be 12 mm. Fig. 7 illustrates the developed FE model and the boundary conditions used in this study. The contact between the specimen and the end block was defined using a node-to-surface contact pair. The top surface of the block constituted the master surface while the edges of the channel were defined as a node-based slave surface. The contact normal to the surface was defined as "hard", meaning that no penetration of the surfaces into each other was allowed. However, the slave nodes on the specimen were allowed to separate from the surface while no tensile stresses could be developed in the interface. The tangential properties were set to "rough", indicating that friction restrained any tangential slip between the specimen and the hinge endplate. This reflects the actual test condition where the end sections were not allowed to expand laterally due to the Poisson effect as a result of friction. Besides, in the experimental test set up, four steel dowels were bolted into the top plates to hold the corners of the channels in place and prevent possible slip.

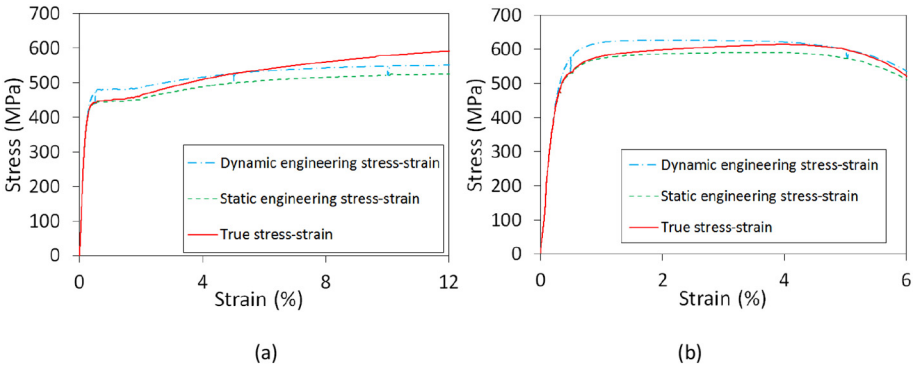

Fig. 6. Stress–strain curves resulted from (a) flat (A01F) and (b) corner coupon tests (A03C and A04C tested in pair).

To simulate the actual behaviour of the supports, contact pairs were defined between the roller and the endplate using a surface-to-surface contact property. This is to take into account the possible effects of the friction on the axial capacity of the CFS elements measured in the experimental tests. In the reference experimental tests discussed in Section 5, lubricating oil was used in order to reduce the friction effect that might produce restraints on the rotation of the endplate. Therefore, in the normal direction of the contact surface, 'hard' property was used while in the tangent direction between the roller and the endplate, a friction factor was used. To obtain the most appropriate friction factor a sensitivity analysis was conducted by varying the friction properties between the roller and the endplate. Friction factors ranging from 0.1 to 0.4 were used and the corresponding relationships between axial load versus axial shortening were obtained as shown in Fig. 8. The results indicate that the effect of friction factor on the rotational behavior of the CFS column can be considerable. It is shown that the predicted compressive capacity decreases with the reduction of friction factor, whereas no significant drop of the peak load is observed using friction factors smaller than 0.2. Also, compared to the model with a friction factor of 0.1, the friction factor 0.2 can lead to better convergence in the numerical study. It will be shown in the following sections that a friction factor of 0.2 provides an excellent agreement between the predicted compressive strengths and the experimental results.

6.3. Element type and mesh size

In the FE models, from the available ABAQUS element library [10], a four-node shell element with reduced integration (S4R) was used, which has three translational and three rotational degrees of freedom at each node. This element accounts for finite membrane strains and arbitrarily large rotations, and therefore, is suitable for large-strain analyses and geometrically non-linear problems. Since the plate components constituting the CFS cross-sections are very slender, transverse shear deformations were not deemed to have a major effect on the solution. Nevertheless, they are accounted for in the S4R element formulation.

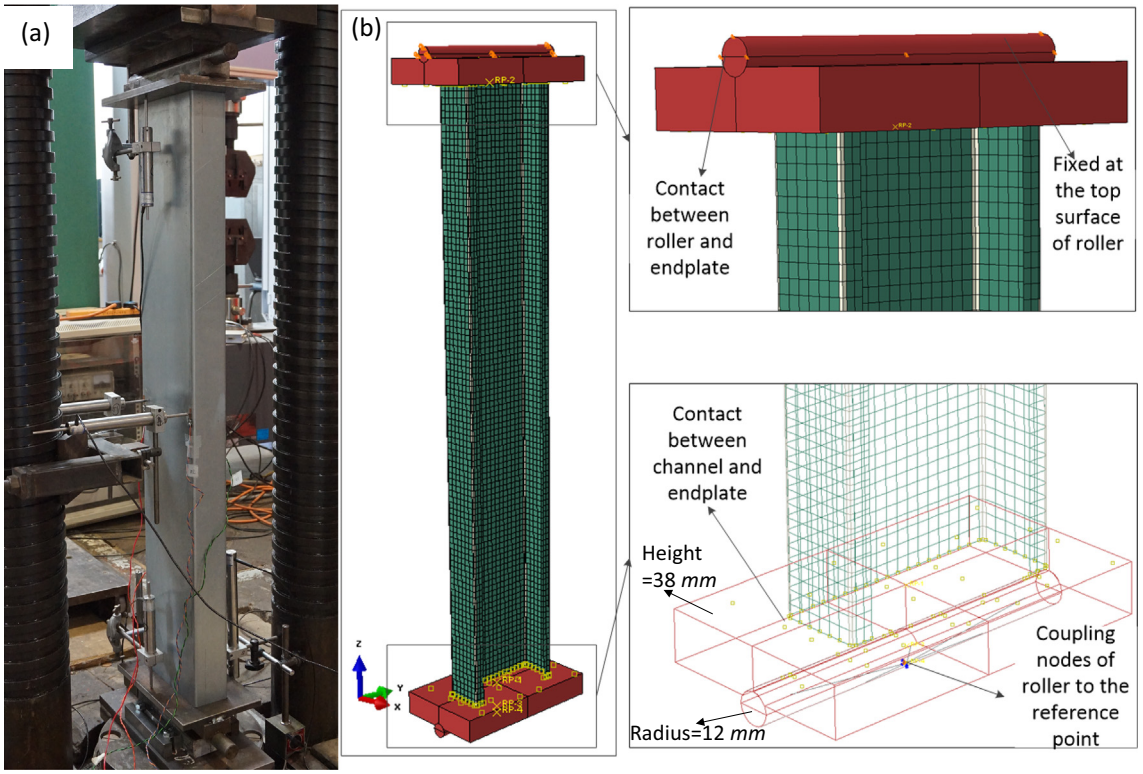

Fig. 7. (a) Experimental test set-up and (b) Developed FE model and boundary condition.

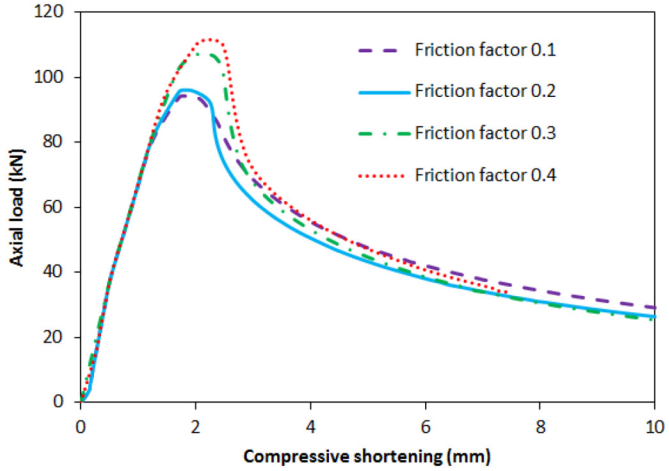

Fig. 8. Axial load vs shortening of A1000-a specimen with various friction factors defined in the contact properties of FE analyses.

For the modeling of the endplate and the roller support, an 8-node linear brick element with reduced integration (C3D8R) and hourglass control (i.e. comparing the energy contained in the zero energy modes with the internal energy of the system) was used [10]. A sensitivity analysis was performed to choose an appropriate mesh size to model the CFS channel sections. The mesh size of the endplate and the roller support was found to have little effects on the peak capacity of the channel sections; however, it could affect the convergence of the FE analyses. It was found that using a 10×10 mm element dimension for CFS channel and $5 \times 5 \times 5$ mm for the linear brick element provides a balance between computational time and accuracy.

6.4. Imperfections

The stability of thin-walled CFS members may in some cases be significantly affected by the presence of geometric imperfections, especially when interactive buckling of different modes is involved [32,33]. Before conducting the experimental tests, the initial geometric imperfections of the test specimens were measured along the five longitudinal lines indicated in Fig. 9 (a), by means of a specially designed set-up with laser displacement transducers. In a first step, the raw data was decomposed into their respective Fourier series [32,33]. The Fourier series were then filtered by cutting off the high-frequency vibrations originating from the driving mechanisms of the moving motors. This has resulted in a smoother profile when the measured imperfections were included. As an example, Fig. 9 shows the measured imperfections of specimen A1000-a along lines ① to ⑤. The readings recorded along lines ①, ② and ③ provide data on the imperfections relevant for overall flexural buckling and local buckling of the web, while the readings along lines ④ and ⑤ provide information about the imperfections affecting the distortional buckling mode.

It should be noted that it is essential to use a significant number of Fourier terms to represent the shape of the measured imperfections accurately. In this study, 10–50 Fourier terms were used by a trial and error process, depending on the length of the specimen. As an example, Fig. 10 displays the measured imperfection profile along line ③ of specimen A1000-a, with the truncated Fourier representation with 20 terms shown as a solid black line.

In a given cross-section, the magnitude of the imperfection at the location of each node of the FE mesh was determined by interpolation of the measured data. Quadratic interpolation was used for the web imperfections, while linear interpolation was used at the flanges, as shown in Fig. 11. Finally, the coordinates of each node of the FE model were adjusted to account for the imperfections. Following the above procedures, a program was developed in Matlab [34] for the inclusion of measured imperfections and generating of nodal coordinates in ABAQUS [10]. To improve the accuracy of the predictions, the small eccentricities of the applied loads (e_0) were also measured and incorporated in the FE models by offsetting the modelled specimen relative to the centroid of the end blocks by a distance of e_0.

6.5. Numerical results

Fig. 12 compares the axial load-axial shortening relationship for A1000-a and C1000-b specimens obtained from the reference

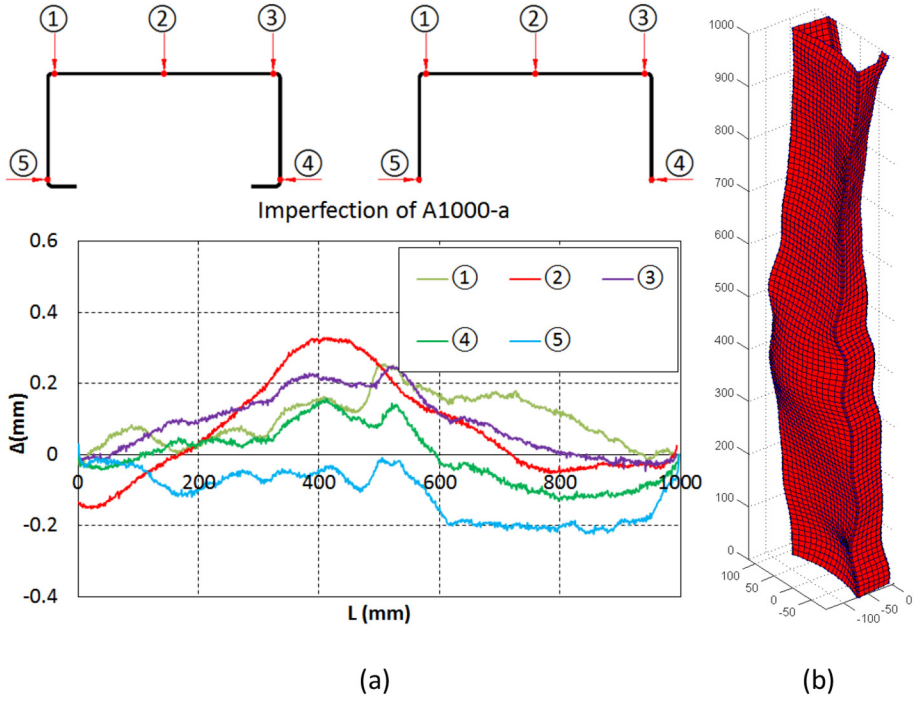

Fig. 9. (a) The measured imperfection profiles; (b) Incorporating measured imperfections for FE models (deformed shape generated in Matlab [34]).

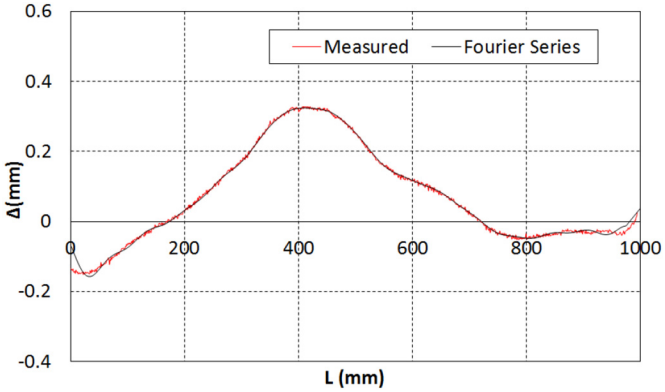

Fig. 10. Measured imperfection profile and its Fourier representation with 20 terms, along line ③ of specimen A1000-a.

experimental tests and the predicted results from the numerical study. It is shown that the proposed FE model was able to capture the peak load, initial stiffness and post buckling behaviour of both CFS plain and lipped channel columns with a very good accuracy. The columns tested in the reference experimental programme all exhibited a local buckling which was then followed by interactive local and flexural buckling failure modes [20,28]. Fig. 13 demonstrates the good agreement between the failure mode and the post-peak deformations of specimen A1000-a observed in the experimental tests with the results of the corresponding FE model at different loading stages. Similar results were obtained for the other test specimens.

Table 2 compares the ultimate load carrying capacity P_u resulting from the detailed FE models with the results obtained from the experiments on the CFS plain and lipped channels. P_{u1} is the predicted axial strength that takes into account the strain hardening effect of the material in the corner regions, while a simplified method is used to incorporate the geometric imperfections by applying a small perturbation force of 10 N horizontally in the middle height of the column [35]. P_{u2} represents the predicted capacity through FE analysis where only the effect of the measured geometric imperfections was taken into account. The predicted capacity P_{u3}, on the other hand, considers both the measured imperfections and the strain hardening effect of the material in the corner regions.

It should be noted that the existing imperfection data (as recorded in Fig.9) may provide only a limited representation of the expected imperfections in standard CFS sections. Therefore, for comparison purposes, new FE models were developed by considering the magnitudes of the local and distortional imperfections based on the cumulative distribution function (CDF) values proposed by Schafer and Peköz [30]. CFD value of 50% was considered, with values of 0.34 t and 0.94 t for local and distortional imperfections, respectively. A value of L_e/1500 was also used for the overall buckling imperfection magnitude. The local, distortional and overall buckling modes were generated using the CUFSM finite strip software [24].The local and distortional imperfections were multiplied with a scale factor and superimposed. The predicted axial capacity values, in this case, are signified as P_{u4} in Table 2.

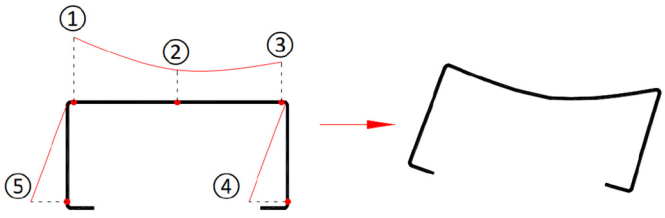

Fig. 11. Inclusion of measured geometric imperfections.

As shown in Table 2, the average ratio of the FE predicted load capacity P_u to the experimentally measured load carrying capacity P_u was 1.114, with a standard deviation of 0.191. This implies that the simplified method used to take into account the geometric imperfections generally led to overestimated (up to 46%) results especially for CFS plain channels. In general, a significantly better agreement was obtained between the FE predictions and the experimental results when the measured imperfections were taken into account. The average ratio of the FE predicted load capacity P_{u2} to the experimentally measured load carrying capacity P_u was 0.985, with a standard deviation of 0.066. In comparison, the average ratio of the FE predicted load capacity P_{u3} to the experimentally measured load carrying capacity P_u was 0.994, with a standard deviation of 0.067. Using the imperfection magnitudes proposed by Schafer and Peköz [30], the average ratio of the FE predicted load capacity P_{u4} to the experimentally measured load carrying capacity P_u was 0.975, with a standard deviation of 0.112. This implies that, by considering the measured imperfections and the strain hardening effects, the developed FE models could predict the actual capacity of the lipped and plain columns with the highest accuracy. However, the use of the imperfection magnitudes proposed by Schafer and Peköz [30] provided an acceptable accuracy for the prediction of axial capacity in practical applications.

It is worth noting that the method of applying a small perturbation force [35] to generate imperfection is a trial and error process, while the use of the imperfection magnitude proposed by Schafer and Peköz [30] provided a more quantitative way to characterize imperfections.

A comparison between the P_{u2} and P_{u3} results indicates that the strength variation caused by the strain hardening of the material in the corner regions in the current test series was not significant (on average <1%). The main reason for the low contribution of the strain hardening can be the relatively small area of the rounded corners compared to the total cross section area in the tested specimens. On the other hand, by comparing the predicted axial strength P_{u1} with P_{u3}, it is shown that the magnitude and the distribution of geometric imperfections can have significant effects on the predicted load carrying capacity (up to 20% and 40% variation for lipped and plain channels, respectively).

7. Accuracy of EC3 and DSM design methodologies

The experimental results listed were compared with the predictions of the DSM and EC3 design equations presented in Sections 2 and 3. As shown in Table 3, in general, the DSM predictions for CFS lipped channel columns are found to be more accurate than the effective width method in EC3. The ratio of the DSM predicted load capacity to the corresponding experimentally measured value was on average 0.945, with a standard deviation of 0.081. In comparison, the average of the predicted axial load capacities using EC3 design method to the experimental results was 0.792, with a standard deviation of 0.07.

It is also evident that the EC3 design method generally leads to considerably more conservative predictions of the column axial load capacity of lipped channels. In almost all cases, the EC3 predictions were lower than the actual strength values obtained from the experimental tests. However, it is shown that DSM results are slightly overestimated for the columns with Type B cross-section. While DSM is not qualified for the design of CFS plain channel columns, it is seen from Table 3 that the EC3 is extremely conservative in the prediction of the axial capacity of the plain channel sections (type C), for which the average ratio of the predicted values to the test results is only 0.38 (see the predicted values in brackets of Table 3).

In order to improve the accuracy of the predictions, the Annex E of EN1993-1-5 [17] presented in Section 2.4 was used, which allows the effective area to be calculated by using the actual stress level at global buckling, rather than at the yield stress. The results obtained after iterations are listed in Table 3. It is seen that the improved EC3 method provides considerably more accurate prediction on the axial capacity of the

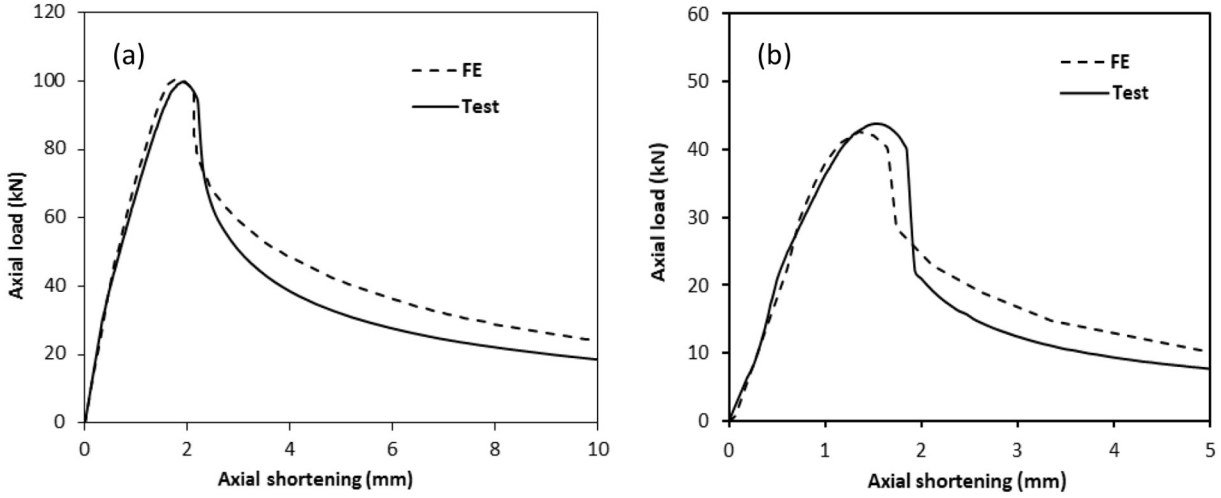

Fig. 12. Axial load-axial shortening relationship resulting from FE against reference experimental tests (a) A1000-a (lipped channel) and (b) C1000-b (plain channel) specimens.

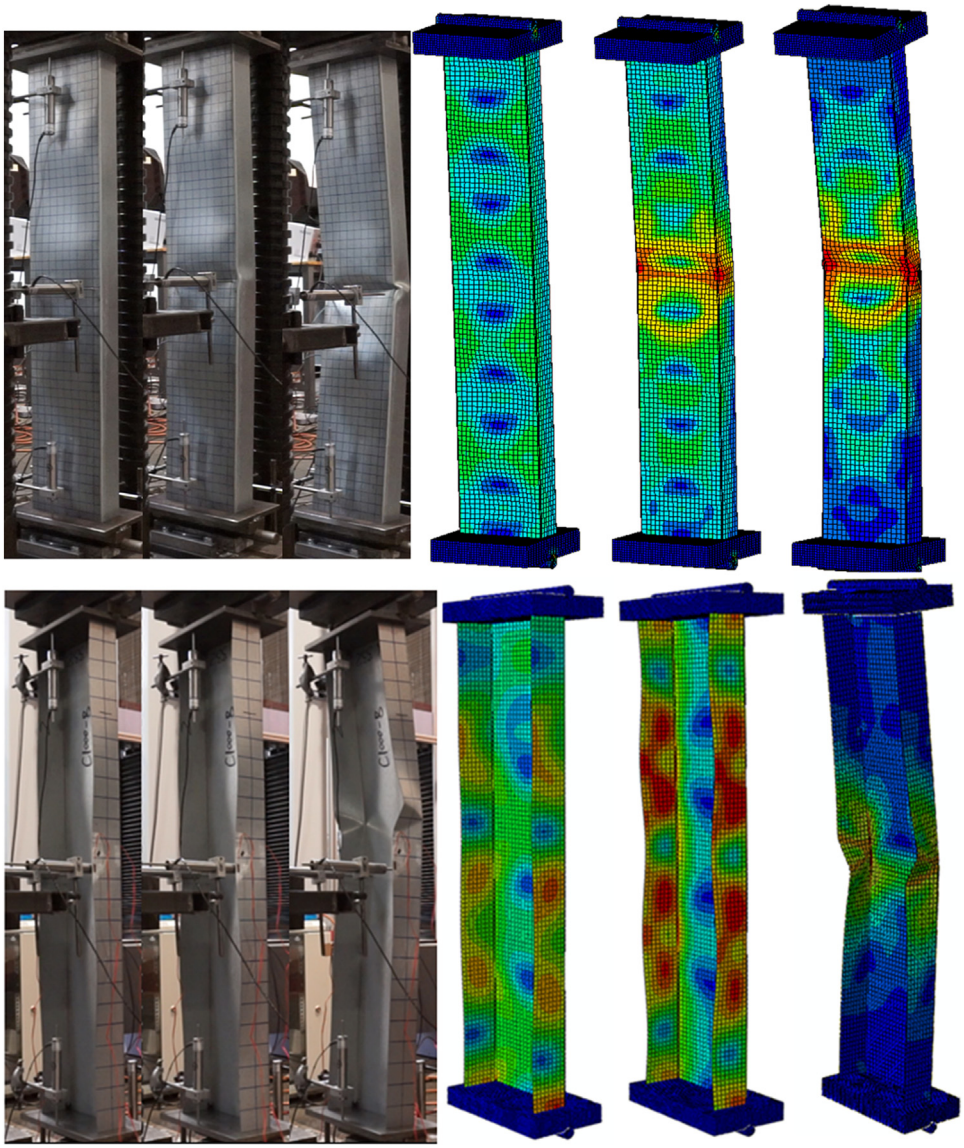

Fig. 13. Deformation pattern and failure mode obtained from FE models vs experimental results at different load levels (A1000-a and C1000-b).

Table 2
Comparison of FE results with tested compressive strength.

Specimen	Length (mm)	P_u (test) (kN)	P_{u1} (FE) (kN)	P_{u2} (FE) (kN)	P_{u3} (FE) (kN)	P_{u4} (FE) (kN)	P_{u1}/P_u	P_{u2}/P_u	P_{u3}/P_u	P_{u4}/P_u
A1000-a	1000.1	99.8	113.7	97.2	97.4	103.8	1.139	0.974	0.976	1.040
A1000-b	1000.0	98.3	117.5	97.0	97.8	103.2	1.195	0.987	0.995	1.050
A1000-c	1000.0	98.7	114.9	96.4	97.4	103.5	1.164	0.977	0.987	1.049
A1500-a	1499.8	95.1	89.8	91.9	92.7	90.09	0.944	0.966	0.975	0.947
A1500-b	1500.0	85.3	81.9	81	81.7	78.08	0.960	0.950	0.958	0.915
A1500-c	1500.0	91.4	94.06	87.6	88.1	87.2	1.029	0.958	0.964	0.954
A2000-a	1999.8	78.4	88.4	75.1	76.2	74.8	1.128	0.958	0.972	0.954
A2000-b	2000.0	75.8	68.0	72.2	73.4	70.4	0.897	0.953	0.968	0.929
A2000-c	2000.1	88.8	70.8	85.8	86.5	83.0	0.797	0.966	0.974	0.935
B1000-a	1000.2	113.8	109.8	114.2	114.7	108.6	0.965	1.004	1.008	0.954
B1000-b	1000.0	110.3	112.5	114.2	114.6	113.1	1.020	1.035	1.039	1.025
B1000-c	1000.1	107.7	110.1	108.3	109.2	109.7	1.022	1.006	1.014	1.019
B1500-a	1500.0	103.8	103.8	108.1	108.4	106.0	1.000	1.041	1.044	1.021
B1500-b	1500.4	107.9	108.3	109.6	110.0	114.9	1.004	1.016	1.019	1.065
B1500-c	1500.1	106.2	108.0	108.3	108.8	108.8	1.017	1.020	1.024	1.024
B2000-a	2000.1	99.6	95.6	102.2	103	105.6	0.960	1.026	1.034	1.060
B2000-b	2000.3	101.6	111.5	105.5	106.2	110.4	1.097	1.038	1.045	1.087
B2000-c	2000.1	105.3	113.3	108.3	109.1	100.3	1.076	1.028	1.036	0.953
(C1000-a)	1000.1	33.6	60.9	–[a]	–[a]	–[a]	–[a]	–[a]	–[a]	–[a]
C1000-b	1000.1	43.8	61.6	42.2	42.5	46.9	1.406	0.963	0.970	1.071
C1000-c	999.8	42.7	60.2	44.1	44.6	46.2	1.410	1.033	1.044	1.082
C1500-a	1500.0	36.3	43.7	33.5	33.6	31.3	1.204	0.923	0.926	0.862
C1500-b	1500.1	35.2	51.1	32.8	32.9	34.1	1.452	0.932	0.935	0.969
C1500-c	1500.2	37.1	54.0	35.6	35.7	34.9	1.456	0.960	0.962	0.941
C2000-a	2000.4	33.1	34.9	29.5	29.9	25.4	1.054	0.891	0.903	0.767
C2000-b	2000.3	31.7	34.8	28.1	28.9	24.0	1.098	0.886	0.912	0.757
C2000-c	2000.0	33.8	36.1	29.9	30.6	25.8	1.068	0.885	0.905	0.763
D1000-a	1000.0	109.0	129.4	106.0	107.0	101.8	1.187	0.972	0.982	0.934
D1000-b	1000.2	110.8	125.4	109.1	112.2	104.1	1.132	0.985	1.013	0.940
D1000-c	1000.1	109.3	130.1	108.0	108.7	102.2	1.190	0.988	0.995	0.935
D1500-a	1500.2	95.0	100.3	94.2	94.6	90.7	1.056	0.992	0.996	0.955
D1500-b	1500.1	98.2	104.5	101.5	101.9	94.5	1.064	1.034	1.038	0.962
D1500-c	1500.0	99.6	101.9	98.1	99.7	95.6	1.023	0.985	1.001	0.960
D2000-a	2000.3	90.8	96.1	86.4	86.9	82.7	1.058	0.952	0.957	0.911
D2000-b	2000.0	97.8	94.2	93.3	94.2	93.1	0.963	0.954	0.963	0.952
D2000-c	2000.1	89.6	93.9	85.8	85.9	81.8	1.048	0.958	0.959	0.924
Average							1.114	0.985	0.994	0.975
St. deviation							0.191	0.066	0.067	0.112

[a] C1000-a experienced a sudden impact from the other machine in the lab during the test.

plain channels (the average ratio of the predicted values to the test results is increased to 0.73).

8. Evaluation of the optimisation process

In this section, the experimental and numerical results are used to assess the efficiency of the optimisation framework previously presented by Ye et al. [16] and briefly summarized in Section 4. As discussed before, cross-section A is a standard commercially available cross-section, while cross-section B is the optimum solution with the highest axial load capacity subject to the design and manufacturing constraints in Eq. (16)–(18). Both cross-sections had an identical coil width and thickness and thus used the same amount of material. The nominal cross-sectional dimensions of these sections are given in Fig. 5.

Fig. 14 compares the ultimate capacity of the standard and the optimised sections for the 1 m, 1.5 m and 2 m length columns obtained from the experimental results, detailed FE models and EC3 design method.

The results in general show that the optimised lipped channel section (type B) offers a considerably higher compressive capacity compared to the standard lipped channel section (type A) with the same amount of material. This improvement is particularly evident in longer columns where global buckling is the dominant mode. Based on the validated FE results, after considering all design and manufacturing constraints, the adopted optimisation method could increase the compressive capacity of the 1 m, 1.5 m and 2 m long columns by 16%, 25% and 35%, respectively. The increase axial capacity in the numerical study for the three lengths are also much the same as shown in the experimental results [28], as shown in Fig. 14. It is worth noting that the trends of increasing/decreasing capacity over the range of lengths for the columns are very well predicted by EC3 when the experimentally validated FE results are taken as a benchmark. This confirms the efficiency of the adopted optimisation method based on EC3 design procedure.

The results of this study, in general, demonstrate the accuracy and reliability of the developed FE models to predict the axial load bearing capacity of CFS columns with different cross-sectional shapes and effective lengths. These validated models should prove useful in practical applications for more efficient design of CFS structural elements.

9. Summary and conclusions

The interaction of local and global buckling in CFS lipped and plain channel columns was studied using detailed nonlinear FE models. The developed models take into account the non-linear stress–strain behaviour of CFS material, the strength hardening effects at the rounded corner regions due to the cold-working process, and the measured initial geometric imperfections. The FE models were validated against a comprehensive experimental program on a total number of 36 plain and lipped channel columns with three different lengths (1 m, 1.5 m and 2 m) and four different cross-sections. The validated models were then used to assess the accuracy of EC3 and DSM design methods for standard and optimum design solutions. Based on the results presented in this paper, the following conclusions can be drawn:

(1) The compressive strength of the sections predicted by the detailed FE models was on average <1% different from the experimental results. The proposed FE model was also successful in

Table 3
Evaluation of the EC3 and DSM design methods against experimental results.

Specimen	Member length (mm)	P_u (test) (kN)	EC3 (kN)	DSM (kN)	EC3/P_u	DSM/P_u
A1000-a	1000.1	99.8	78.2	92.3	0.784	0.925
A1000-b	1000.0	98.3	79.4	93.2	0.808	0.948
A1000-c	1000.0	98.7	77.8	91.5	0.788	0.927
A1500-a	1499.8	95.1	71.5	81.7	0.752	0.859
A1500-b	1500.0	85.3	68.9	78.6	0.808	0.921
A1500-c	1500.0	91.4	71.6	81.7	0.783	0.894
A2000-a	1999.8	78.4	59.6	65.4	0.760	0.834
A2000-b	2000.0	75.8	58.7	64.2	0.774	0.847
A2000-c	2000.1	88.8	59.8	65.4	0.673	0.737
B1000-a	1000.2	113.8	98.3	119.4	0.864	1.049
B1000-b	1000.0	110.3	98.1	118.9	0.889	1.078
B1000-c	1000.1	107.7	92.2	113.7	0.856	1.056
B1500-a	1500.0	103.8	89.5	108.7	0.862	1.047
B1500-b	1500.4	107.9	91.0	111.4	0.843	1.032
B1500-c	1500.1	106.2	92.1	110.9	0.867	1.044
B2000-a	2000.1	99.6	78.7	94.8	0.790	0.952
B2000-b	2000.3	101.6	81.9	98.6	0.806	0.970
B2000-c	2000.1	105.3	82.0	98.5	0.779	0.936
C1000-a	1000.1	33.6	26.3 (14.8)	NA	0.783 (0.440)	–[a]
C1000-b	1000.1	43.8	25.5 (14.4)	NA	0.582 (0.328)	–[a]
C1000-c	999.8	42.7	26.2 (14.7)	NA	0.614 (0.344)	–[a]
C1500-a	1500.0	36.3	26.5 (14.0)	NA	0.730 (0.386)	–[a]
C1500-b	1500.1	35.2	26.5 (13.9)	NA	0.753 (0.395)	–[a]
C1500-c	1500.2	37.1	26.1 (13.7)	NA	0.704 (0.369)	–[a]
C2000-a	2000.4	33.1	26.2 (12.7)	NA	0.792 (0.384)	–[a]
C2000-b	2000.3	31.7	26.7 (12.9)	NA	0.842 (0.407)	–[a]
C2000-c	2000.0	33.8	25.6 (12.3)	NA	0.757 (0.364)	–[a]
D1000-a	1000.0	109.0	90.1	102.82	0.827	0.943
D1000-b	1000.2	110.8	92.3	105.39	0.833	0.951
D1000-c	1000.1	109.3	92.8	106.21	0.849	0.972
D1500-a	1500.2	95.0	83.7	94.48	0.881	0.995
D1500-b	1500.1	98.2	86.3	97.92	0.879	0.997
D1500-c	1500.0	99.6	84.4	95.67	0.847	0.961
D2000-a	2000.3	90.8	71.4	79.22	0.786	0.872
D2000-b	2000.0	97.8	73.4	82.16	0.751	0.840
D2000-c	2000.1	89.6	73.8	82.36	0.824	0.919
Average					0.792	0.945
St. deviation					0.070	0.081

Numbers in the brackets are without considering the iterations suggested by Annex E of EN1993-1–5.
[a] Unpredefined sections for DSM.

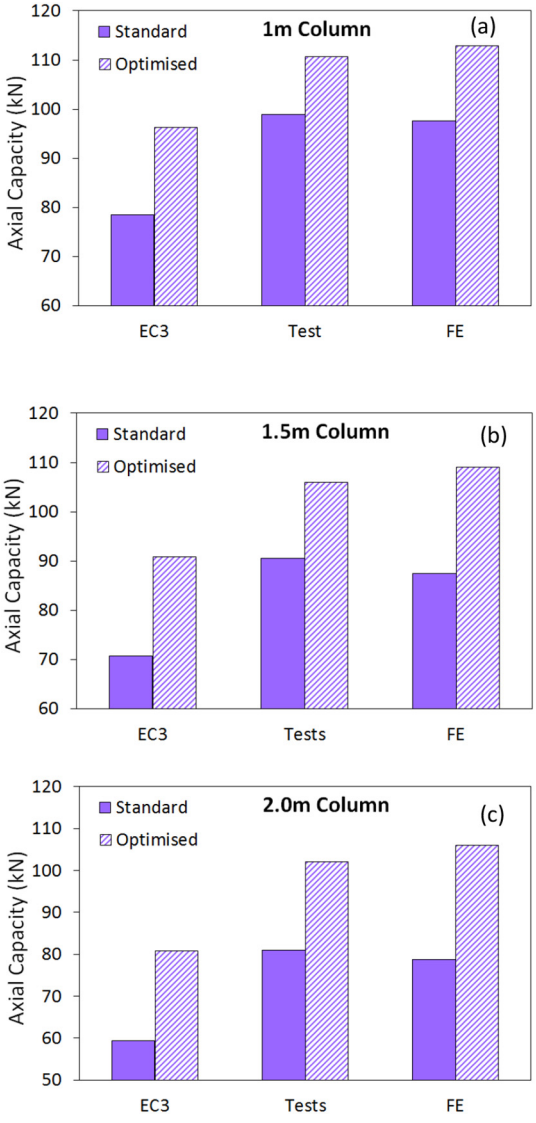

Fig. 14. Comparison between the compressive strength of the standard (Type A) and the optimised (Type B) lipped channels using the same amount of material.

capturing the initial stiffness, failure shapes and post buckling behaviour of CFS columns subjected to local and global buckling modes.

(2) It was shown that the initial geometric imperfections can change the FE predictions by around 20% and 40%, respectively, for lipped and plain channel columns, while the strength variation caused by the strain hardening effect at the rounded corner zones, in general, has negligible effects (<1%).

(3) The ratio of predicted to experimentally measured axial strength was on average 0.95 and 0.79 for DSM and EC3 design methods, respectively. The results show that EC3 design method generally leads to conservative predictions, especially for plain channel column sections where the EC3 predictions were up to 62% lower than the experimental results. However, by using the Annex E of EN1993-1–5 to calculate the effective cross-section based on the actual stress level rather than the yield strength, the accuracy of the predictions was significantly improved.

(4) The results demonstrated the efficiency of the adopted optimisation method to improve the compressive capacity of CFS sections. The axial capacity of the optimised CFS columns obtained from experimental tests and validated FE models were up to 35% higher than their standard lipped channel counterparts with the same amount of material. This improvement was more evident for longer columns where global buckling was the dominant failure mode.

Acknowledgments

This work was supported by the EPSRC grant EP/L019116/1. The authors would like to thank the EPSRC for their financial support. The authors also would like to express their gratitude to BW Industries for providing the test specimens free of charge.

References

[1] L. Fiorino, O. Iuorio, R. Landolfo, Designing CFS structures: the new school BFS in Naples, Thin-Walled Struct. 78 (2014) 37–47.
[2] J.B.P. Lim, D.A. Nethercot, Ultimate strength of bolted moment-connections between cold-formed steel members, Thin-Walled Struct. 41 (11) (2003) 1019–1039.
[3] J.B.P. Lim, D.A. Nethercot, Finite element idealization of a cold-formed steel portal frame, J. Struct. Eng. ASCE 130 (1) (2004) 78–94.
[4] A. Van der Neut, The interaction of local buckling and column failure of thin-walled compression members, Applied Mechanics, Springer 1969, pp. 389–399.
[5] A. Van der Neut, The sensitivity of thin-walled compression members to column axis imperfection, Int. J. Solids Struct. 9 (8) (1973) 999–1011.
[6] B. Young, J. Yan, Finite element analysis and design of fixed-ended plain channel columns, Finite Elem. Anal. Des. 38 (6) (2002) 549–566.
[7] B. Young, Design of channel columns with inclined edge stiffeners, J. Constr. Steel Res. 60 (2) (2004) 183–197.
[8] J. Yan, B. Young, Numerical investigation of channel columns with complex stiffeners - part I: test verification, Thin-Walled Struct. 42 (6) (2004) 883–893.

[9] B. Young, J. Yan, Numerical investigation of channel columns with complex stiffeners - part II: parametric study and design, Thin-Walled Struct. 42 (6) (2004) 895–909.
[10] ABAQUS 6.13, Analysis user's guide, Dassault Systems, 2013.
[11] Y.C. Zhang, C.G. Wang, Z.N. Zhang, Tests and finite element analysis of pin-ended channel columns with inclined simple edge stiffeners, J. Constr. Steel Res. 63 (3) (2007) 383–395.
[12] ANSYS, User's Guide, Release 14.5, Ansys Inc., Canonsburg, 2012.
[13] C.A. Wang, Z.N. Zhang, D.Q. Zhao, Q.Q. Liu, Compression tests and numerical analysis of web-stiffened channels with complex edge stiffeners, J. Constr. Steel Res. 116 (2016) 29–39.
[14] D. Ayhan, B.W. Schafer, Characterization of in-plane backbone response of cold-formed steel beams, J. Constr. Steel Res. 132 (2017) 141–150.
[15] W. Ma, J. Becque, I. Hajirasouliha, J. Ye, Cross-sectional optimization of cold-formed steel channels to Eurocode 3, Eng. Struct. 101 (2015) 641–651.
[16] J. Ye, I. Hajirasouliha, J. Becque, A. Eslami, Optimum design of cold-formed steel beams using Particle Swarm Optimisation method, J. Constr. Steel Res. 122 (2016) 80–93.
[17] CEN, Eurocode 3: Design of Steel Structures, Part 1–5: Plated structural elements, Brussels, European Comittee for Standardization, 2005.
[18] CEN, Eurocode 3: Design of Steel Structures, Part 1-3: General Rules—Supplementary Rules for Cold Formed Members and Sheeting, Brussels, European Comittee for Standardization, 2005.
[19] CEN, Eurocode 3: Design of Steel Structures. Part 1-1: General Rules and Rules for Buildings, Brussels, European Comittee for Standardization, 2005.
[20] J. Ye, More Efficient Cold-formed Steel Elements and Bolted ConnectionsPhD thesis The University of Sheffield, 2016.
[21] J. Ye, I. Hajirasouliha, J. Becque, K. Pilakoutas, Experimental investigation of local-flexural interactive buckling of CFS channel columns, Proceedings of the 7th International Conference on Coupled Instabilities in Metal Structures, Baltimore, USA, 2016.
[22] B. Young, K.J.R. Rasmussen, Design of lipped channel columns, J. Struct. Eng. ASCE 124 (2) (1998) 140–148.
[23] AISI, North American Specification for the Design of Cold-formed Steel Structural Members, 2007 Edition AISI S100-07, Washington, DC, 2007.
[24] B. Schafer, CUFSM Version 3.12, Department of Civil Engineering, Johns Hopkins University, 2006, http://www.ce.jhu.edu/bschafer/cufsm/.
[25] S. Adany, B.W. Schafer, Buckling mode decomposition of single-branched open cross-section members via finite strip method: Derivation, Thin-Walled Struct. 44 (5) (2006) 563–584.
[26] S. Adany, B.W. Schafer, Buckling mode decomposition of single-branched open cross-section members via finite strip method: application and examples, Thin-Walled Struct. 44 (5) (2006) 585–600.
[27] J. Ye, I. Hajirasouliha, J. Becque, K. Pilakoutas, Development of more efficient cold-formed steel channel sections in bending, Thin-Walled Struct. 101 (2016) 1–13.
[28] J. Ye, I. Hajirasouliha, J. Becque, Experimental investigation of local-flexural interactive buckling of cold-formed steel channel columns, Thin-Walled Struct. (2018) (accepted).
[29] BS EN ISO 6892-1, Metallic materials Tensile testing Part 1: Method of test at room temperature, Brussels: European Committee for Standardization, 2009.
[30] B. Schafer, T. Peköz, Computational modeling of cold-formed steel: characterizing geometric imperfections and residual stresses, J. Constr. Steel Res. 47 (3) (1998) 193–210.
[31] Y. Huang, B. Young, The art of coupon tests, J. Constr. Steel Res. 96 (2014) 159–175.
[32] J. Becque, K.J. Rasmussen, Numerical investigation of the interaction of local and overall buckling of stainless steel I-columns, J. Struct. Eng. ASCE 135 (11) (2009) 1349–1356.
[33] J. Becque, K.J. Rasmussen, Experimental investigation of local-overall interaction buckling of stainless steel lipped channel columns, J. Constr. Steel Res. 65 (8) (2009) 1677–1684.
[34] V. MATLAB, 7.10. 0 (R2010a), MathWorks, Natick, MA, 2010.
[35] J. Meek, S. Loganathan, Large displacement analysis of space-frame structures, Comput. Methods Appl. Mech. Eng. 72 (1) (1989) 57–75.